IOP Publishing Biomed. Mater. 20 (2025) 065002 https://doi.org/10.1088/1748-605X/ae084b

Biomedical Materials

PAPER

Inorganic polyphosphate, a paradigm changer in 3D printing of β-tricalcium phosphate based materials for bone tissue surgery

Meik Neufurth[1], **David Molter**[1], **Xiaoqin La**[2], **Changxin Wu**[2], **Hiroshi Ushijima**[3], **Heinz C Schröder**[1], **Xiaohong Wang**[1,*] and **Werner E G Müller**[1,*]

[1] ERC Advanced Investigator Grant Research Group at the Institute for Physiological Chemistry, University Medical Center of the Johannes Gutenberg University, Duesbergweg 6, 55128 Mainz, Germany

[2] Institutes of Biomedical Sciences, the Key Laboratory of Chemical Biology and Molecular Engineering of Ministry of Education of China, Key Laboratory of Medical Molecular Cell Biology of Shanxi Province, Shanxi University, Taiyuan 030006, People's Republic of China

[3] Nihon University, Division of Microbiology, Department of Pathology and Microbiology, Nihon University-School of Medicine, Tokyo, Japan

[*] Authors to whom any correspondence should be addressed.

E-mail: wang013@uni-mainz.de and wmueller@uni-mainz.de

Keywords: inorganic polyphosphate, β-tricalcium phosphate, 3D-printing, regenerative activity, mesenchymal stem cells, biomineralization

OPEN ACCESS

RECEIVED
25 July 2025

REVISED
8 September 2025

ACCEPTED FOR PUBLICATION
17 September 2025

PUBLISHED
3 October 2025

Abstract

β-Tricalcium phosphate (β-TCP) is widely used as a material for bone implants due to its excellent biocompatibility, biodegradability, and osteoconductivity, as well as its osteoinductive properties. Here, we demonstrate that the regenerative potential of this material can be significantly enhanced when incorporated into a matrix of inorganic polyphosphate (polyP), a physiological, metabolically active polymer composed of phosphate residues linked by high-energy phosphoanhydride bonds. A 3D-printable hydrogel was developed containing suspended β-TCP and amorphous calcium-polyP nanoparticles (Ca-polyP-NP; the water-insoluble depot form of polyP), as well as NaH_2PO_4 as the monomeric precursor of the polymeric, water-soluble Na-polyP. Heating the printed scaffold to 700 °C causes condensation of NaH_2PO_4, resulting in the formation of a Na-polyP glass melt that embeds the Ca-polyP-NP and β-TCP particles. The final scaffolds exhibited the necessary porosity, with pore sizes ranging from 10 to 100 µm (average 84 µm), which are suitable for bone ingrowth, along with the required mechanical stability. The morphogenetically active polyP component is released from the 3D-printed porous scaffolds in appropriate amounts, significantly increasing both the proliferation and energy-dependent differentiation of mesenchymal stem cells (MSCs) into mineralizing osteoblasts compared to polyP-free β-TCP scaffolds. Moreover, enhanced formation of collagen fibers and hydroxyapatite deposits on the cell surface, as well as accelerated microvessel tube formation, were observed in MSCs seeded on polyP-containing scaffolds. These results demonstrate that the novel strategy of integrating β-TCP with polyP as an energy-supplying, regeneration-promoting component imparts superior functional properties to β-TCP scaffolds, making them a promising material for future bone implant applications.

1. Introduction

Autogenous bone grafts are considered the 'Gold Standard' for the treatment of segmental bone defects (reviewed in [1]). Historically, other biominerals were used to repair damage, such as sponges in plastic surgery, e.g. as a nose substitute [2]. Even more straightforward and optimistic in his vision was Vallesii–Covar [3], who claimed to approach the regenerative potential for bone defects in his chapter 'De dentinuo regeneratione.'

Importantly, biomaterials for tissue engineering must be biocompatible—meaning they should not induce adverse tissue reactions and should preferably

interact with the host in a beneficial and appropriate manner [4]. However, if such a material is used as a porous scaffold, it does not necessarily stimulate the biological regenerative process and may lead to the formation of functionally useless tissue [5, 6]. Therefore, *in vivo* performance—such as degradation, mechanotransduction, and tissue matrix expression—is crucial for the quality of a biomaterial and must align with its biocompatibility. To meet these requirements, a biomaterial should possess regenerative activity and ideally be replaced by physiological granulation tissue: regenerated connective tissue interspersed with microscopic blood vessels that supply the newly formed tissue in the healing area.

The implant material should support the regeneration-promoting activities of damaged osteochondral tissue. This presents a particular challenge for the body because bone and cartilage are functionally two distinct specialized forms of connective tissue and are both low in cell density [7]. A naturally produced, well-understood intrinsic component is bone morphogenetic proteins (BMPs) [8].

Implants are used to physically stabilize and—preferably—induce regeneration in damaged or injured organs. A physiological polymer that consistently accumulates at injury sites or regions undergoing differentiation is polyphosphate (polyP) [9, 10]. PolyP is a biological inorganic polymer present in every cell, with the highest concentrations found in blood platelets and macrophages [11, 12]. These cells transport polyP through the bloodstream to target sites such as bone fractures [13] or bone formation areas [14, 15].

Physiological polyP is a distinguished implantable biomaterial characterized by the following beneficial properties identified both *in vitro* and *in vivo*. Cellular experiments in artificial environments (culture medium/serum) have shown that polyP: *(i)* is biocompatible and biodegradable [16], even in co-polyP nanocarrier form; *(ii)* is osteoinductive and chondroinductive by stimulating alkaline phosphatase (ALP) expression in bone-mineralizing cells [17, 18], and promotes chondrogenesis by inducing cytokine expression, indicating its significant role in chondrocyte metabolism [19]; *(iii)* possesses template-forming ability via transformation into a coacervate phase [20].

During coacervation, polyP undergoes liquid–liquid phase separation in the presence of Ca^{2+} in aqueous solution, forming a dense aqueous phase in thermodynamic exchange with a dilute phase [21].

Every regenerative process in the body, including BMP7-mediated induction, depends on metabolic energy (adenosine triphosphate, ATP), which is dissipated during anabolic reactions [22, 23]. To date, polyP is the only biomaterial identified that can generate ATP extracellularly [24]. PolyP is released from activated platelets [25], for instance, via thrombin [26].

Once released into the extracellular space, polyP appears either as soluble Na-polyphosphate (Na-polyP) or as Ca-polyphosphate nanoparticles (Ca-polyP-NP). There, it is enzymatically hydrolyzed by ALP to release orthophosphate (P_i) [27], cleaving individual P_i residues linked via high-energy phosphoanhydride bonds [10]. As predicted by Lipmann [28], free energy from catabolic reactions is stored in such energy-rich bonds as in ATP. Experiments with hydroxyapatite (HA)-producing SaOS-2 cells showed that extracellular polyP leads to ADP generation via AMP phosphorylation [29].

Consequently, *in vitro* studies investigated whether polyP and the subsequent ATP generation affect energy-dependent cell migration, such as microvessel formation [30] during initial vascularization and myofibroblast migration during wound healing [31]. These studies convincingly demonstrated that initial microvascularization depends on enzymatic conversion of polyP to ATP [32]. Depleting ATP using apyrase prevents microvessel formation. A second effect of ATP is its chemotactic guidance of endothelial cells [32, 33]. The role of ATP in myofibroblast migration was confirmed through histological studies of these cells during wound healing [34].

Animal studies, building upon *in vitro* findings, must be evidence-based and scientifically validated per the Animal Welfare Act [35] before human application. The most promising medicinal regenerative activities of polyP were studied *in vivo* in two directions: as a bone healing polymer and as a wound healing/skin regeneration polymer—both reaching proof-of-concept.

In the present study, we asked whether the favorable properties of β-TCP as a 3D-printable bone implant material—particularly its stability, osteoconductivity, and osteoinductivity—can be enhanced by supplementation with polyP, and whether this can extend to energy supply needs in regenerative processes. However, polyP, especially in its biologically active soluble form, as Na-polyP, is prone to hydrolysis during ink processing and post-printing sterilization via autoclaving [36]. Therefore, we developed a thermal procedure where Na-polyP is formed after printing by heating the scaffold (initially containing NaH_2PO_4) at 700 °C as introduced [37]. Furthermore, Ca-polyP-NP—more stable and functioning as a depot form of polyP requiring protein

contact to form biologically active coacervates [20]—were directly incorporated into the hydrogel-based ink used in this study. The resulting 3D scaffolds were compared to β-TCP scaffolds regarding their physical/chemical and *in vitro* biological properties.

2. Materials and methods

2.1. Materials

Na-polyP, with an average chain length of 40 phosphate (P_i) units, was purchased from Chemische Fabrik Budenheim (Budenheim, Germany).

2.2. Fabrication of the scaffold by 3D bioprinting

The dry mixture consisted of 1200 mg sodium phosphate monobasic (NaH_2PO_4; Sigma, Taufkirchen, Germany), 300 mg Ca-polyP-NP (prepared as described by Müller *et al* [38]), 150 mg κ-carrageenan (Sigma #22048), 45 mg xanthan gum from *Xanthomonas campestris* (Sigma #G1253), and 1305 mg β-tricalcium phosphate (β-TCP; Sigma #49963). This dry blend was combined with 2454.5 mg of distilled water to yield a final weight of 5454.5 mg. The mixture was thoroughly homogenized and transferred into a syringe. After standing overnight, 6 ml of the bubble-free printing paste was loaded into a cartridge and mounted onto a pre-warmed (20 °C) 3D printing head.

Printing was conducted with a 3D Bioplotter (fourth generation blotter; Envisiontec, Gladbeck; Germany) through a 1.8 mm blunt cannula, connected with the printer head, at 0.5 bar pressure and a printing speed of 18 mm s^{-1}, resulting in gel cylinders measuring 13 mm in diameter and 1.5 mm in height as outlined before (figure 1) [39, 40]. The scaffold stacks composed of NaH_2PO_4/Ca-polyP-NP, κ-carrageenan, xanthan gum, and β-TCP (polyP-κ-Car-Xan-β-TCP) were pre-designed using the software Perfactory RP 3.2.

The printed stacks were frozen at—80 °C for 1 h and subsequently freeze-dried overnight to induce pore formation. The pore structure was stabilized by sintering the samples at 700 °C for 1 h [41]. Scaffolds were routinely washed three times with medium before use. These samples were used for scanning electron microscopy (SEM), X-ray diffraction (XRD), porosity, and cell biology analyses. β-TCP served as the control material.

In some experiments, scaffolds were printed without polyP (i.e. omitting Ca-polyP-NP and NaH_2PO_4 as precursors for condensed Na-polyP), using only β-TCP, κ-carrageenan, and xanthan gum. These dry components were again mixed with distilled water to reach a final weight of 5454.5 mg.

2.3. Mechanical properties—Nanoindentation

Surface mechanical properties of the scaffolds were assessed by nanoindentation using the NanoTest Vantage System (Micro Materials Ltd, Wrexham, UK), equipped with a Berkovich diamond indenter [42]. At least 50 independent indentations were performed per sample under the following conditions: temperature 25 °C, maximum indentation depth 1 µm, loading/unloading rate 0.3 mN s^{-1}, and a holding time of 30 s at maximum load. The distance between adjacent indentations was maintained at a minimum of 30 µm.

Martens hardness (HM) and the reduced Young's modulus (Er) were calculated from the raw data according to established methods [42]. Calculations were performed using Nano-Test Platform Four V.40.08 software (Micro Materials Ltd, Wrexham, UK).

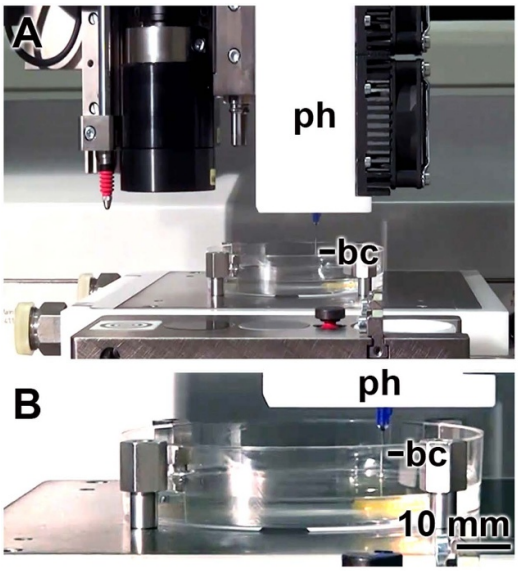

Figure 1. The 3D bioplotter used for this study. (A) The apparatus with the printer head (ph) and blunt cannula (bc). (B) The printing outflow at higher magnification.

2.4. Mechanical properties—Compression testing

Bulk mechanical performance was evaluated via ultimate compression testing [43] using the 'MultiTest 2.5-xt Force Testing System' with a 2500 N Load cell unit (Mecmesin Ltd., Slinfold, UK). Samples were compressed longitudinally at 1 mm min^{-1} using a 50 mm load-disc until failure. Force, displacement, and time data were recorded continuously at 1 kHz using the Emperor XT Force software (Mecmesin Ltd.). Young's modulus (E) and ultimate compressive strength (UCS) were calculated from the data.

2.5. PolyP release from the stacks

PolyP release was quantified using the Phosfinity Quant Kit (Aminoverse B.V., HK Nuth, The Netherlands), as described [44]. One scaffold disk per well was placed in 24-well plates containing 1 ml PBS and incubated at 37 °C with 5% CO_2. At specified time points, 500 µl of supernatant was collected and analyzed after enzymatic hydrolysis with

yeast exopolyphosphatase, followed by colorimetric detection of orthophosphate. Phosphate concentrations were determined from a standard curve. Each value represents data from five independent experiments. PBS supernatants from incubated stacks were stored frozen until further use in viability and *in vitro* mineralization assays.

2.6. Porosity, density, and pore size determination

Pore size and distribution were assessed via capillary flow porometry (1200-AEHXL, Porous Media Inc., Ithaca, NY), a non-destructive method using non-reactive gas flow through dry samples [45, 46]. Data analysis was performed using Porous Media software.

Porosity was determined using a water pycnometer, as described by Matko *et al* [47].

Implant density was measured using a BELPYCNO L device (Microtrac Retsch, Haan, Germany).

2.7. Cell biological studies

Human mesenchymal stem cells (MSC; Lonza, Cologne, Germany) were cultured in 75 cm^2 flasks using serum-free StemPro MSC SFM XenoFree medium (Invitrogen-Thermo Fisher, Dreieich, Germany) at 37 °C in a humidified incubator.

Cell proliferation and viability assays: MSCs (passage < 9) were seeded at 5×10^3 cells cm^{-2} in 24-well plates. One printed scaffold disk was added per well and incubated for up to 6 d before sub-culturing. For longer experiments, the medium was replaced every 3–4 d with fresh medium and supplements as needed.

Viability was assessed using the PrestoBlue assay (#A13261; Invitrogen-Thermo Fisher), following the method described by Gloeckner *et al* [48]. After 2 h of dye incubation, fluorescence was measured at 569 nm. Ten replicates were performed, and data are presented as mean ± SD ($^*p < 0.01$). Viable MSCs overgrowing the scaffold grids were stained with Calcein-AM (#17783; Sigma), as described by White *et al* [49].

***In vitro* mineralization assay:** MSCs were differentiated into mineralizing osteoblasts by incubating them in differentiation medium for 9 d, containing a mineralization activation cocktail (5 mM β-glycerophosphate, 50 mM ascorbic acid, and 10 nM dexamethasone), as established by Müller *et al* [38] and others [50–53].

To evaluate mineralization on cell surfaces, MSCs were cultured on plastic coverslips (Nunc-Thermo Fisher Scientific, Dreieich, Germany) in StemPro medium. After 9 d, the medium was supplemented with the mineralization cocktail, with or without PBS supernatants from 5 d incubated 3D-printed scaffolds. Mineral deposits were stained using 10% Alizarin Red S (#A5533, Sigma), and quantification was performed spectrophotometrically at 405 nm [54, 55]. Values were normalized to DNA content (measured using PicoGreen; Sigma) according to Schröder *et al* [56].

Mineralizing cells on scaffolds were stained with OsteoImage (Lonza) for HA and with Draq5 (Invitrogen-Thermo Fisher) for nuclear staining.

Type I collagen expression was visualized using a goat anti-collagen I antibody (#AB758; Sigma) and a secondary donkey anti-goat IgG conjugated with Alexa Fluor 488 (ab150129; Abcam, Cambridge, UK).

***In vitro* angiogenesis assay:** 3D-printed scaffolds (with or without polyP) were placed in 24-well plates (#SIAL0524; Sigma) and overlaid with 0.5 ml serum-free StemPro medium. A 1 mm thick layer of Cultrex extracellular matrix (reduced growth factor basement membrane extract; #3445-005-01; Sigma) was added and incubated for 1 h at 37 °C. Then, 3×10^4 MSCs were seeded and incubated for 1–4 d, following Khoo *et al* [57]. Cell arrangements were visualized under an Olympus microscope with Nomarski interference contrast optics.

2.8. Statistical analysis

All results are presented as mean ± SD. Unless stated otherwise, statistical analysis was performed using one-way ANOVA followed by Tukey's post-hoc test. A p-value < 0.05 was considered statistically significant. Quantification was carried out using ImageJ software on high-resolution images. Statistical analysis was conducted using GraphPad Prism software (GraphPad Software Inc.).

3. Results

The scaffold developed in this study goes beyond the capabilities of a conventional scaffold. It not only provides mechanical support and a porous environment that is conducive to cell infiltration, but also delivers osteoinductive stimuli, which are particularly important in the treatment of hard tissue fractures. This latter functionality is provided by the polyP component, which supplies metabolic energy [24] and regenerative potential [58, 59]. What is novel here is that the polymer encapsulates crystalline β-TCP within a polyP shell, significantly enhancing the ceramic's biocompatibility.

3.1. Biomaterial ink composition: organic matrix—Osteoconductive/-inductive β-TCP—Morphogenetic polyP

The biomaterial ink comprises three main components: the organic polymers κ-carrageenan and xanthan gum, the synthetic osteoconductive/-inductive β-TCP, and the physiologically active morphogenetic polyP (including Ca-polyP-NP and NaH_2PO_4 as the precursor to Na-polyP; figure 2). The organic matrix is reinforced with biodegradable β-TCP and the morphogenetically active Na-polyP, formed from NaH_2PO_4 through heating at 700 °C. At

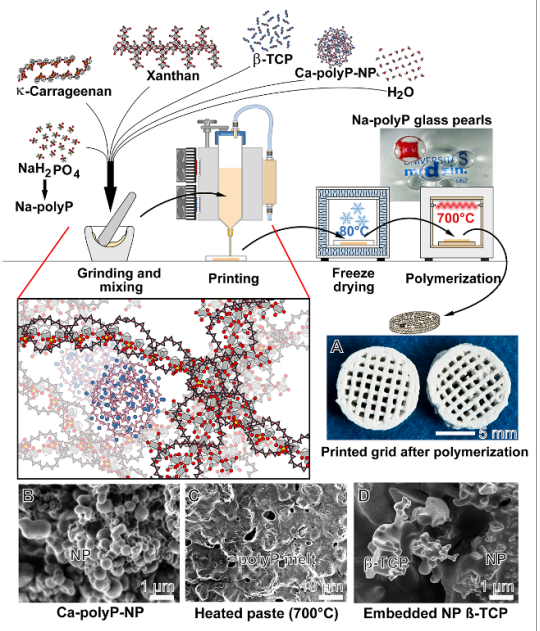

Figure 2. Schematic outline of the preparation of the polyP/β-TCP scaffold. As starting materials, the organic components κ-carrageenan and xanthan gum were used, to which NaH_2PO_4 was added as a precursor for Na-polyP and Ca-polyP-NP together with β-TCP. The printing paste was processed in a 3D-printer by forming the strutted printed grids. After printing, the samples were frozen at −80 °C and subsequently freeze dried to stabilize the structure and induce porosity. Afterwards, the grids were calcinated at 700 °C. (A) Strutted printed grids; light microscopy. During calcination, NaH_2PO_4 is processed to Na-polyP and the formed (C) molten glass envelops (B) the Ca-polyP-NP and (D) β-TCP; SEM.

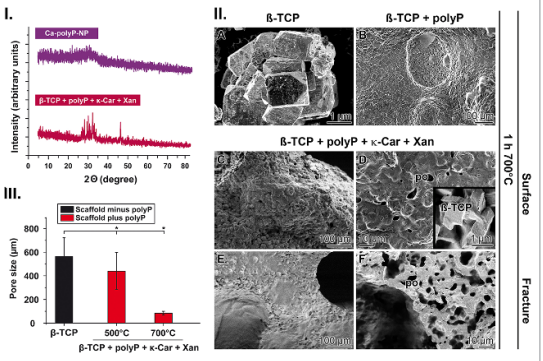

Figure 3. Characteristics of the polyP/β-TCP-κ-carrageenan-xanthan gum scaffold. (I.) XRD patterns of Ca-polyP-NP and of the polymer together with β-TCP in the presence of κ-carrageenan and xanthan gum. (II.) Pore formation within β-TCP, polyP, κ-carrageenan and xanthan gum during calcination (1 h at 700 °C); SEM. β-TCP crystals (A) without and (B) with polyP component. The distribution pattern shows homogeneously distributed crystals. After calcination of the scaffold (β-TCP, polyP, κ-carrageenan, xanthan gum), pores (po) are formed that have a (C and D) smaller diameter on the surface of the printed grids than those (E and F) inside the grids at their fracture edges. (III.) Average pore size of the scaffold composed of β-TCP, minus or plus polyP, at 500 °C and 700 °C. A capillary flow porometer was used for analysis ($n = 6$).

this temperature, NaH_2PO_4 undergoes condensation into longer polyP chains [37].

Physiologically, both Na-polyP and Ca-polyP-NP are generated during platelet formation in megakaryocytes and released at the platelet surface within a Ca^{2+}-rich environment [25, 60]. The Na-polyP in the scaffold is highly soluble in aqueous environments, while Ca-polyP-NP remains stable in water unless exposed to peptides or proteins that lower their ζ-potential [20]. Consequently, Na-polyP elicits immediate biomedical effects, while Ca-polyP-NP acts as a slow-release depot [34].

3.2. 3D printing process

For 3D printing, the organic components, β-TCP, and NaH_2PO_4 were blended with distilled water (0.8-fold wt./wt.) and loaded bubble-free into a cartridge, which was connected to the 3D printing bioplotter. The scaffold was printed with a predefined pattern using PerfactoryRP 3.2 software (EnvisionTEC, Gladbeck, Germany), with settings optimized based on previous work [40]. The printed scaffold discs were frozen at −80 °C to facilitate pore formation and then heated for 1 h at 700 °C.

At this temperature, β-TCP—the most commonly used degradable bone graft material—remains stable and does not convert into α-TCP [61]. Simultaneously, the carbonizing organic matrix promotes internal pore formation. After heating, the scaffold diameter shrinks from 13 mm to 10.4 mm, and the strut diameter from 400 µm to 320 µm (figure 2(A)), dimensions deemed optimal for bioprinting [62]. During heating, the dispersed Ca-polyP-NP and β-TCP become embedded in a molten polyP glass matrix (figures 2(B)–(D)).

3.3. Effect of the organic matrix—Pore size formation

Porosity is essential for implants in hard tissue repair, allowing cell invasion and ECM remodeling. The organic matrix (κ-carrageenan and xanthan gum) forms a hydrogel that enables even dispersion of β-TCP and amorphous Ca-polyP-NP prior to calcination. After heating at 700 °C, the crystallinity of β-TCP decreases substantially in the presence of the organic matrix, forming an almost amorphous phase (figure 3(I))—a beneficial property for implant materials [63]. This behavior is supported by computational studies [64].

At 700 °C, Na-polyP melts and flows around β-TCP particles without forming pores (figures 3(II-A) and (II-B))). However, adding κ-carrageenan and xanthan gum results in the formation of distinct pores ranging from 10–100 µm (figures 3(II-C)–(II-F)). Surface pores are smaller (≈5–10 µm), while internal fracture edge pores are larger (≈80–110 µm).

Capillary flow porometry on dry samples revealed that the pore size around β-TCP decreased from 566 µm in pure β-TCP to 439 µm with added polyP and organic matrix (heated to 500 °C). Upon heating

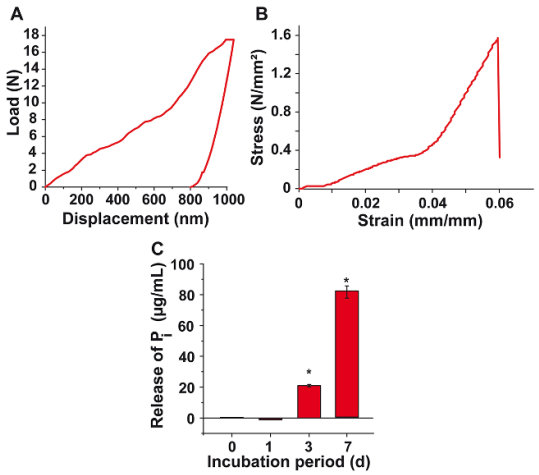

Figure 4. Mechanical properties of the porous β-TCP-polyP scaffold. (A) A typical load-displacement curve for indentation experiments with the scaffold. (B) A representative stress–strain diagram showing the compressive response of the scaffold with increasing force. (C) Release of polyP (expressed as P_i) from one printed disc per well in 24-well plates during a 0–7 d incubation period. Quantitative determinations were performed with the Phosfinity Quant kit assay. ($n = 10$). Significance levels are given ($^*P < 0.001$).

to 700 °C—when polyP melts [65]—average pore size decreased further to 84 µm (figure 3(III)), which is optimal for bone implants [66]. The scaffolds shrank by 35 ± 7% ($n = 6$) during melting. The final porosity was 73 ± 7% ($n = 10$), and the specific density was 1.7 ± 0.3 g cm^{-3} ($n = 10$).

3.4. Mechanical properties

Bone implants must match the mechanical characteristics of surrounding hard and soft tissues while promoting tissue regeneration. The β-TCP/polyP scaffold meets both criteria.

3.4.1. Stiffness

The elastic properties at the bone–implant interface (ranging from fixed, covalent bonding to frictionless contact) are critical for implant stability [67]. A thin, dense bone layer (lamina dura) surrounding the implant ensures biomechanical compatibility [68].

Nanoindentation assessed stiffness of the 3D-printed scaffolds (β-TCP, polyP, and organic matrix). Figure 4(A) shows a representative load-displacement curve. The HM and reduced Young's modulus (Er) were calculated using Nano-Test Platform Four V.40.08 software. A load of ∼17.5 N produced a 1 µm indentation. The curve indicates a hard surface with low elasticity: HM = 0.86 ± 0.24 GPa; Er = 26.41 ± 4.20 GPa—values 8–9 times higher than for human trabecular bone [69]. This is attributed to the polyP glass coating formed during heat treatment. However, stiffness decreases upon cell contact due to polyP release.

3.4.2. Compression testing

Bulk mechanical properties were also tested via compression. Figure 4(B) presents a stress–strain curve. The UCS was 1.72 ± 0.38 MPa, suitable for trabecular bone implants [70, 71]. The elastic modulus (E) was 54.4 ± 9.54 MPa. Initial strain increases (up to 0.04 mm mm^{-1}) are attributed to minor surface defects. A linear stress increase follows until the scaffold fails at ∼1.6 MPa.

3.4.3. PolyP release from the scaffold

One notable property of the porous polyP/β-TCP scaffold is polyP release during MSC culture. PolyP release begins after 3 d (20 µg ml^{-1}) and rises to 83 µg ml^{-1} after 7 d (figure 4(C)). These concentrations are known to stimulate cell proliferation and osteogenic gene expression, including ALP [38, 72].

3.5. Morphogenetic activity

The interface between an implant and the surrounding tissue is a site of intense cell differentiation and proliferation [73], making it an area of high metabolic energy demand. Initial insights into the biocompatibility and bioenergetics of cells growing on 3D-printed grids can be gained by evaluating cell proliferation in relation to changes in polyP levels during the incubation period.

3.5.1. Cell proliferation

The studies were conducted using β-TCP grids printed without the polyP component (β-TCP–κ-carrageenan–xanthan gum and heated to 700 °C) as well as grids containing the polymer and processed by melting. MSCs were seeded onto the grids and incubated in the medium for up to 6 d (figure 5(A)). To correlate the cell growth-promoting effect of polyP [38] with the accumulation of polyP in the medium, soluble Na-polyP was quantified using the Phosfinity assay. During the incubation period, polyP concentrations in the medium rose to 23 µg ml^{-1} after 3 d and 67 µg ml^{-1} after 6 d.

In parallel, MSC growth was quantified using the colorimetric PrestoBlue cell viability assay. On polyP-free scaffolds, cell proliferation increased only slightly from 5 × 10^3 cells cm^{-2} per well after seeding to 10.3 × 10^3 cells cm^{-2} after 6 d (figure 5(A)). In contrast, in wells containing polyP-enriched grids (releasing 23 µg polyP ml^{-1}), cell numbers significantly increased to 17.3 × 10^3 cells cm^{-2} per well after 3 d and reached 24.4 × 10^3 cells cm^{-2} per well after 6 d. As shown in figure 5(A), the differences in cell numbers between the polyP-free and polyP-containing grids are significant at both 3 and 6 d of incubation, during which the polymer concentration in the supernatant increased to 23 µg ml^{-1} and 67 µg ml^{-1}, respectively.

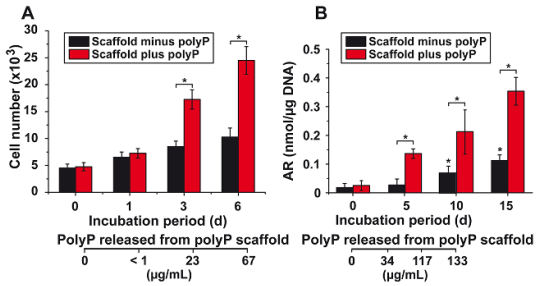

Figure 5. Amplified cell growth and mineralization of MSC on polyP-supplemented β-TCP-based scaffolds. (A) Differences in MSC cell growth on β-TCP-based scaffolds in the presence or absence of polyP supplement. After seeding (day 0), the cells were incubated for 1 d, 3 d, or 6 d in the StemPro MSC SFM medium. After termination, cell number was determined with the colorimetric cell viability PrestoBlue reagent. (B) Change of hydroxyapatite mineralization of cells following incubation of MSC on a scaffold containing β-TCP and polyP. As a reagent to quantify mineralization, Alizarin Red S (AR) was used. The degree of mineralization is given in nanomoles of reagent bound to the cells, correlated with µg of cellular DNA as a measure of cell density. All assays were performed tenfold; the significance is given with a $^*P < 0.001$. The concentration of polyP released into the medium at the different points during the incubation period is shown below in A and B (quantification with the Phosfinity assay).

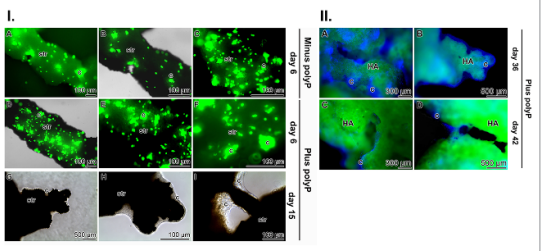

Figure 6. Overgrowth of grids with MSC; fluorescence microscopy. (I.) The cells were vitally stained with Calcein. The cells were seeded on (A to C) β-TCP grids minus polyP or on (D to I) grids that also contained polyP. The fluorescence images show that after an incubation period of 6 d (A to C) significantly less cells (c) are attached on the struts (str) lacking polyP than to those (D to F) enriched with polyP. The light microscopic images (G to I) show that after a period of 15 d the cell layers protrude from the struts. (II.) Intensive mineralization of differentiated MSC on the polyP/β-TCP scaffold. The 3D scaffolds with their cross struts were incubated with the green fluorescent dye OsteoImage [staining for hydroxyapatite (HA)] together with blue reacting Draq5 [flashing the DNA in the cell (c) nuclei] after a total incubation period of 36 d or 42 d. The cells on the polyP/β-TCP scaffold are abundantly covered with HA minerals.

3.5.2. Biomineralization on the cells

During MSC incubation in medium supplemented with a mineralization cocktail (β-glycerophosphate, ascorbic acid, and dexamethasone), the cells begin to express ALP, a key biomarker of osteogenic differentiation [17, 53]. This enzyme indicates the transition of MSCs into the osteoblast stage [74].

MSCs were incubated for 5–15 d in the supplemented medium, with one grid submersed per well. Mineralization was quantified using Alizarin Red S (AR). Cells were seeded onto both polyP-free and polyP-enriched grids. In the latter, polyP levels rose from 34 µg ml^{-1} (day 5) to 133 µg ml^{-1} (day 15). At the time of seeding, mineralization activity was minimal ($<0.03 \pm 0.02$ nmol µg^{-1} DNA), with no detectable polyP in the medium. However, for cells on polyP-containing scaffolds, AR-positive mineral deposits significantly increased to 0.15 ± 0.05 (day 5) and 0.35 ± 0.09 nmol µg^{-1} DNA (day 15) (figure 5(B)). In contrast, cells on polyP-free scaffolds exhibited only modest mineralization, rising from $<0.03 \pm 0.02$ to 0.12 ± 0.04 nmol µg^{-1} DNA by day 15 (not shown).

3.5.3. Overgrowth of printed grids

Regardless of whether the 3D-printed bioink discs contained polyP (as Ca-polyP-NP and Na-polyP) or not, MSCs readily attached to the printed structures (figure 6(I)). To visualize adherent cells or clusters, metabolically active MSCs were stained with Calcein-AM and analyzed via fluorescence microscopy. A clear difference was observed in cell density between polyP-free and polyP-containing β-TCP scaffolds after 6 d. The polyP-free scaffolds exhibited approximately 40% fewer stained cells/clusters (figures 6(I–A to C)) compared to polyP-enriched grids (figures 6(I–D to F)). As mentioned previously, mineralization activity on polyP-containing struts increased consistently over the first 15 d (figure 5(B)). During this period, cells formed a compact layer overgrowing the struts (figures 6(I–G to I)).

3.5.4. Intensive mineralization on differentiated MSCs

As outlined in the 'Introduction,' the incubation medium must be supplemented with a mineralization cocktail to facilitate synthesis of HA and collagen, primarily supported by ascorbic acid and dexamethasone [75]. Ascorbic acid is essential for post-translational hydroxylation via lysine hydroxylase [76], and dexamethasone helps prevent apoptosis during MSC differentiation while accelerating proliferation [77]. Though polyP alone can serve as a P_i source via enzymatic hydrolysis by ALP [78], β-glycerophosphate was also included.

MSC differentiation into osteoblasts is completed after 29 d [75]. Mineralization was visualized using OsteoImage staining after 36 and 42 d. Surprisingly, by day 36, most nuclei (stained blue with Draq5) were already surrounded by green-fluorescing HA deposits (figures 6(II-A) and (II-B))). By day 42, green fluorescence encompassed the entire cell margins (figures 6(II-C) and (II-D))). It is noteworthy that strut diameters decreased by approximately 20%.

3.5.5. Strong expression of collagen fibers together with the mineral phase

Bone is an anisotropic and viscoelastic material. Thus, it is essential to evaluate the induction of the collagen matrix, which imparts elasticity to the mineral phase and allows energy absorption without fracture [79].

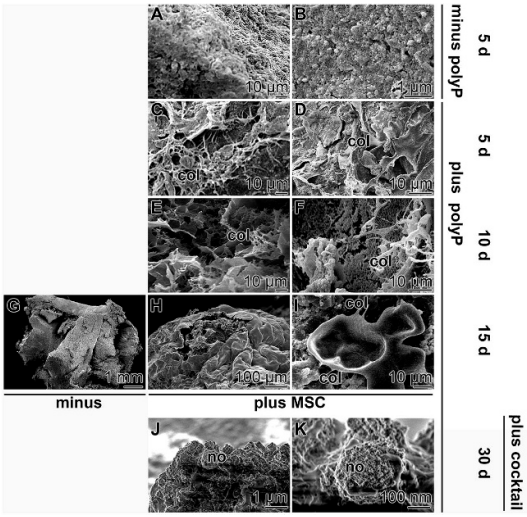

Figure 7. Vigorous collagen synthesis and subsequent HA mineralization of MSC on 3D printed polyP-enriched bioink slices; SEM. (A) and (B) MSC growing on polyP-lacking grids after 5 d of incubation. However, when the cells were seeded on polyP-enriched scaffolds, a time-dependent increase of a surrounding fibrillary collagen (col) net can be seen after (C) and (D) 5 d, (E) and (F) 10 d and (H) and (I) 15 d. (G) After 15 d, the grids began to disintegrate in medium/serum. (J) and (K) subsequent exposure of the 'primed' MSC to the mineralization cocktail induced the cells to form bulky mineral deposits with HA nodules (no).

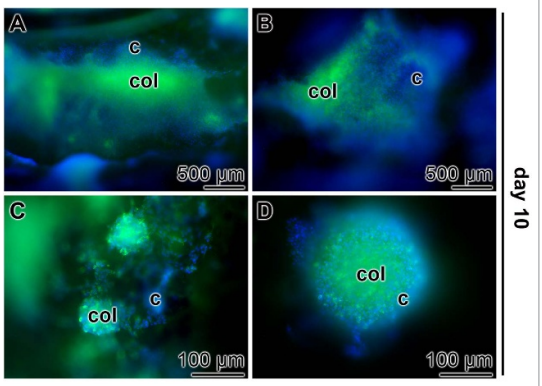

Figure 8. Formation of collagen layers on top of the MSC cell coats; immunofluorescence microscopy. (A) and (B) The cells (c) stained blue with Draq5 are covered with a fibrillar collagen (col) net (stained green with collagen type I antibodies). (C) and (D) The collagen assemblies form clusters on the top of the MSC.

In this study, MSCs capable of producing collagen type I—the predominant collagen in bone [80]—were used. This collagen type is upregulated upon incubation with platelet-rich plasma, a natural polyP source [81]. MSCs seeded onto polyP-free 3D-printed scaffolds exhibited granular surfaces (figures 7(A) and (B)), whereas those on polyP-enriched scaffolds displayed protruding collagen fibrils within 5 d (figures 7(C) and (D)). With continued incubation for 10 and 15 d, the collagen networks thickened (figures 7(E) and (F)), eventually forming mats (figures 7(H) and (I)). Over time, scaffold struts began to disintegrate (figure 7(G)).

Following 15 d of incubation, MSCs on polyP scaffolds were further cultured in mineralization medium until day 30. During this period, substantial mineral deposition occurred, resulting in large (>100 µm) solid nodules (figures 7(J) and (K)).

To confirm the presence of collagen networks, immunofluorescence staining with collagen type I antibodies (green) and Draq5 (blue) for cell nuclei was performed. At day 10, the collagen mats substantially covered the MSC layer (figures 8(A) and (B)). High-magnification images revealed collagen fibrils forming clusters over the cells (figures 8(C) and (D)).

In a previous review, we summarized that MSC in the presence of polyP express the mineralization marker RUNX2 (runt-related transcription factor 2—transcription factor), OCN (osteocalcin—signaling molecule), the enzyme ALP, and the angiogenic growth factor vascular endothelial growth factor [10]. All molecules have a common denominator and reflect increased HA expression and synthesis in cells or tissues; all of these increased markers can be detected by the OsteoImage stain. Therefore, this staining method was used in this study because, unlike polymerase chain reaction, it allows for clear documentation of whether expression levels in a specific cell layer are only speckled or–this is important here–extensive. This staining techniques has been applied for RUNX2 [82], OCN [82], ALP [83] and even collagen [84].

3.6. Accelerated tube formation by MSC on polyP-supplemented scaffold

As reported previously, MSCs were seeded onto a thin extracellular matrix layer [32]. In these experiments, the polyP polymer needed to diffuse from the scaffold through the surrounding medium and matrix to reach the cells. Consequently, tube formation was only observed after 2 d and even more so after 3 d of incubation (figures 9(A)–(C)). By day 4, complete tubular structures had formed and were clearly visible (figure 9(D)).

In contrast, the control group—scaffolds printed without polyP—showed no such development. Even after 4 d, the cells had not formed any complete tubular structures, and no circular formations were observed (figure 9(E)).

4. Discussion

β-TCP is a well-established bone graft substitute [85]. In addition to its osteoconductive properties, β-TCP also exhibits osteoinductive potential, largely attributed to its surface characteristics and porosity

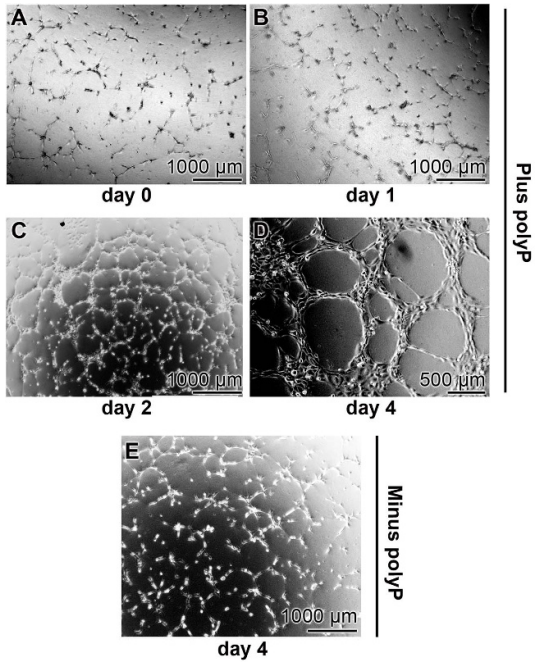

Figure 9. PolyP addition to the β-TCP scaffold accelerates tube formation. MSC were seeded on a thin extracellular matrix layer. Tube formation on the polyP-containing scaffold on day (A) 0, (B) 1, (C) 2 and (D) 4. On day 4, complete tubes can be seen. (E) Control; cells on a scaffold without polyP, after 4 d.

[86, 87]. The biomechanical properties of β-TCP have been improved by implementing the 'Binder Jetting technology', in which the objects are formed by additive manufacturing. In this technique, 3D printed and manufactured objects are formed by layer-by-layer deposition of a liquid binder onto a powder bed [88]. Comparable stability was achieved using polyetheretherketone composites reinforced with polytetrafluoroethylene and nano-sized alumina nanowire, particularly when the latter components were present at a concentration of 10% and 5% by wt., respectively [89].

Polyetheretherketone is already used in patients for spinal implants, highlighting the high biocompatibility of this polymer [90].

Certain β-TCP preparations exhibit Ca-rich, alkaline surface phases that attract mesenchymal stem cells (MSCs), which subsequently grow into these regions, especially when the material is submerged in osteogenic medium [86]. This phenomenon, where bone formation is induced at heterotopic (ectopic) sites, has been termed intrinsic osteoinduction [91]. It should not be confused with osteogenic induction [92], a developmental process involving signal-mediated differentiation of uncommitted osteoprogenitor cells into specialized bone cells (osteoblasts and osteocytes) in the absence of any material influence [87].

Importantly, this differentiation process is highly energy-intensive [93]. At this critical point, polyP proves to be a valuable factor for the success of implants for bone restoration and repair. PolyP acts as an energy-delivery system [24], the potential of which has not yet been fully exploited in implantology. Its metabolism—catalyzed by the cell surface-associated enzymes ALP and adenylate kinase (ADK) [59]—leads to ATP production in the extracellular space. This is a key feature because both bone formation and bone regeneration occur extracellularly [94], although ATP concentrations in this compartment are very low (~10 nM), in contrast to the intracellular levels of 3–10 mM [95].

PolyP can be polymerized from sodium dihydrogen phosphate (NaH_2PO_4) to amorphous Na-polyP at temperatures above 600 °C [96]. In the current study, this thermal process was employed to encapsulate thermally stable β-TCP in the fluid polyP melt. For 3D printing the implants, geometries were computer-modeled, and the printing ink was formulated by combining NaH_2PO_4 and β-TCP with hydrogel-forming polymers—xanthan gum and κ-carrageenan. This ink composition enabled the production of bubble-free implants with precise architecture. Upon heating to temperatures above 600 °C, Na-polyP was formed, and the β-TCP structures became enwrapped in the polymer matrix. Concurrently, this thermal treatment conferred mechanical strength and established a porous internal architecture.

The resulting pore sizes ranged from 10–100 µm—ideal for bone ingrowth—and above 150 µm for osteon formation [97], supporting applications in both *in vivo* bone regeneration and *in vitro* bone marrow MSC cultures [66]. Studies have demonstrated that scaffold porosity comparable to human trabecular bone (70%–90%) enhances both cell viability and bone ingrowth [98]. The scaffolds developed in this study showed a porosity of 70%–75%, which is well within this favorable range for osteogenesis [99].

A particularly notable finding was the specific density of the polyP-κ-carrageenan-xanthan-β-TCP implants: approximately 1.7 ± 0.3 g cm^{-3}. This is significantly lower than the density of pure β-TCP (~3.0 g cm^{-3} [100];), and closely aligns with the density of natural bone (~1.5 g cm^{-3} [101];).

In terms of mechanical properties, the HM of the printed implants was ~0.9 GPa, aligning well with the requirements for human bone implants [69]. The measured UCS of 1.7 ± 0.38 MPa is also suitable for use in trabecular bone implantation [70, 71]. PolyP release from the implants—incubated in PBS at 37 °C for 7 d—reached concentrations of ~80 µg ml^{-1}, a level known to promote both growth and morphogenetic activity [10]. The elastic modulus of the polyP-κ-Car-Xan-β-TCP material was found to be ~54.4 MPa, which is within the broad range observed for different skeletal regions [102]. Therefore, and this is important, the flexibility of the implants is more similar to embryonic bone before age-related bone hardening.

The ideal goal of bone implants is for them to be gradually resorbed and replaced by newly formed tissue. The resorbability of polyP-based materials has been demonstrated experimentally [103]. Animal models revealed that polyP, when encapsulated in poly(*D,L*-lactide-*co*-glycolide) microspheres, is completely replaced by native tissue within six weeks. In contrast, β-TCP remains present in the defect site, as it is insoluble under physiological conditions and is only resorbed by osteoclasts following local acidification [85]. It is worth noting that during the thermal processing of the polyP-β-TCP composite, a shrinkage of ~20% occurs. Thus, the initial dimensions of the 3D-printed scaffolds must be adjusted accordingly [104].

In conclusion, the most advantageous feature of the polyP-κ-Car-Xan-β-TCP composite implant is its enhanced osteoinductive capability, derived from the morphogenetic activity of polyP and its unique role as an extracellular metabolic energy source—an attribute unmatched by any other known implant material. PolyP is a diffusible inducer capable of stimulating gene expression in both prokaryotic [105] and eukaryotic systems [24]. In eukaryotes, polyP activates the mTOR (mammalian target of rapamycin) signaling pathway—specifically the mTORC1 and mTORC2 complexes—which are central to promoting growth and cell survival [106]. Among other functions, mTORC1 regulates ribosome biogenesis, as well as RNA and protein synthesis [107]. The emerging significance of polyP as a bioavailable energy source has recently been underscored by analyses that break down its contributions into metabolic, mechanical, and thermal energy [108].

5. Conclusion

Innovative strategies for the design—and ideally also for the treatment and regeneration—of bone defects increasingly involve the use of stem cells combined with scaffolds that support and enhance mechanical stability at the site of injury [109, 110]. In general, during the regenerative phase, cells—whether self-replicating or differentiating into other lineages—are activated by solute molecules or ions, such as growth factors or hormones, which guide them toward their functional roles [111].

PolyP and its derivatives such as Na-polyP and Ca-polyP nanoparticles (Ca-polyP-NP) are known to transform into a soluble phase by coacervation [20]. PolyP polymers are highly biocompatible and clinically safe, as demonstrated by Proof-of-Concept applications in our studies on chronic wound healing [34, 112] and alveolar cleft repair [113]. These studies underscored the safety of the physiological polymer polyP in patients. Furthermore, polyP has been deemed safe by both the U.S. Food and Drug Administration (FDA) and the European Union (EU). The polymer has been assigned the E-numbers E452i for Na-polyP, E452iii for Na/Ca-polyP, and E452iv for Ca-polyP [114]. The distinguished feature and property of polyP is that, unlike any metallic, inorganic or organic implants, polyP-supplemented implants release ATP, the energy-rich metabolite known to be essential for all regenerative processes in the human body [24, 59].

In the present study, we demonstrate that the novel scaffold composed of polyP-κ-carrageenan-xanthan-β-TCP, following thermal processing, releases soluble polyP in concentrations sufficient to exert morphogenetic activity on the surface of the 3D-printed implants.

These scaffolds are colonized by human MSC, which not only exhibit vigorous proliferation but also remarkable differentiation into osteoblasts. The osteoblasts subsequently initiate the formation of HA-like minerals. This observation highlights the inherent suitability of β-TCP/polyP composites as bone implant materials. While β-TCP contributes the necessary mechanical stability, the polyP component provides potent morphogenetic signaling.

In addition, polyP, together with the cell-surface-associated enzymes ALP and ADK [115, 116], fulfills a dual function: it acts as a phosphate donor through enzyme-mediated hydrolysis and simultaneously supports the extracellular generation of the metabolic energy carrier ATP [24].

Data availability statement

The data cannot be made publicly available upon publication because they contain commercially sensitive information. The data that support the findings of this study are available upon reasonable request from the authors.

Acknowledgments

We thank Ms. Kerstin Bahr, Institute of Functional and Clinical Anatomy, University Medical Center of the Johannes Gutenberg University, Mainz (Germany) for continuous support. W.E.G. M. is the holder of an ERC Advanced Investigator Grant (Grant No. 268476). In addition, W.E.G. M. has obtained three ERC-PoC grants (Si-Bone-PoC, Grant No. 324564; MorphoVES-PoC, Grant No. 662486; and ArthroDUR, Grant No. 767234). Further support came from the BMBF (Chinese-German cooperation in industry-led collaborative projects; 'SKIN-ENERGY'—FKZ 13GW0403B). Finally, this work was supported by grants from the European Commission (Grant Nos. 604036 and 311848), the International Human Frontier Science Program, and

the BiomaTiCS research initiative of the University Medical Center, Mainz.

Author contributions

Meik Neufurth 0000-0002-2383-6412
Conceptualization (lead), Data curation (lead), Investigation (lead), Methodology (lead), Project administration (equal), Supervision (equal), Validation (equal), Visualization (equal), Writing – original draft (equal), Writing – review & editing (equal)

David Molter
Data curation (equal), Investigation (equal), Methodology (equal), Validation (equal), Visualization (equal), Writing – review & editing (supporting)

Xiaoqin La
Data curation (equal), Investigation (equal), Methodology (equal), Validation (equal), Visualization (equal), Writing – review & editing (supporting)

Changxin Wu 0000-0002-7416-1662
Conceptualization (supporting), Methodology (supporting), Supervision (supporting), Validation (supporting), Visualization (supporting), Writing – review & editing (supporting)

Hiroshi Ushijima
Conceptualization (supporting), Investigation (supporting), Methodology (supporting), Supervision (supporting), Validation (supporting), Visualization (supporting), Writing – review & editing (supporting)

Heinz C Schröder 0000-0003-0992-6427
Conceptualization (equal), Methodology (equal), Supervision (equal), Validation (equal), Visualization (equal), Writing – original draft (equal), Writing – review & editing (equal)

Xiaohong Wang 0000-0003-1796-6314
Conceptualization (lead), Data curation (lead), Investigation (lead), Methodology (lead), Project administration (lead), Supervision (lead), Validation (lead), Visualization (lead), Writing – original draft (lead), Writing – review & editing (lead)

Werner E G Müller 0000-0002-8223-3689
Conceptualization (lead), Data curation (lead), Formal analysis (lead), Funding acquisition (lead), Methodology (lead), Project administration (lead), Resources (lead), Supervision (lead), Visualization (lead), Writing – original draft (lead), Writing – review & editing (lead)

References

[1] Meeder P J and Eggers C 1994 The history of autogenous bone grafting *Injury* **25** A2–3
[2] Camper P 1771 *Naauwkeurige Afbelding En Beschryving van Eene Geheel En Al Verloorene, Maar Door Kunst Herstelde Neus En Verhemelte* (Seep–Boekverkooper)
[3] Vallesii-Covar F 1606 *Controuersiarum Medicarum et Philisophicarum* (Wechelianis apud Claud. Marnium) pp 75
[4] Anderson J M 2012 *Biocompatibility. Polymer Science: A Comprehensive Reference* ed K Matyjaszewski and M Möller (Elsevier) pp 363–83
[5] Williams D F 2017 A paradigm for the evaluation of tissue-engineering biomaterials and templates *Tissue Eng. C* **23** 926–37
[6] Wang X H, Schröder H C and Müller W E G 2014 Enzymatically synthesized inorganic polymers as morphogenetically active bone scaffolds: application in regenerative medicine *Int. Rev. Cell Mol. Biol.* **313** 27–77
[7] Foldager C B, Gomoll A H, Lind M and Spector M 2012 Cell seeding densities in autologous chondrocyte implantation techniques for cartilage repair *Cartilage* **3** 108–17
[8] Katagiri T and Watabe T 2016 Bone morphogenetic proteins *Cold Spring Harb Perspect. Biol.* **8** a021899
[9] Wang Y, Li M, Li P, Teng H, Fan D, Du W and Guo Z 2019 Progress and applications of polyphosphate in bone and cartilage regeneration *BioMed Res. Int.* **2019** 5141204
[10] Wang X H, Schröder H C and Müller W E G 2018 Amorphous polyphosphate, a smart bioinspired nano-/bio-material for bone and cartilage regeneration: towards a new paradigm in tissue engineering *J. Mater. Chem. B* **6** 2385–412
[11] Schröder H C and Müller W E G (ed) 1999 Inorganic Polyphosphates; Biochemistry, Biology, Biotechnology (*Progress in Molecular and Subcellular Biology*) vol 23 (Springer)
[12] Kulaev I S, Vagabov V and Kulakovskaya T 2004 *The Biochemistry of Inorganic Polyphosphates* 2nd edn (Wiley)
[13] Serbest S, Tiftikçi U, Tosun H B, Gümüştaş S A and Uludag A 2016 Is there a relationship between fracture healing and mean platelet volume? *Ther. Clin. Risk Manag.* **12** 1095–9
[14] Wirth F, Huck K, Lubosch A, Zoeller C, Ghura H, Porubsky S and Nakchbandi I A 2021 Cdc42 in osterix-expressing cells alters osteoblast behavior and myeloid lineage commitment *Bone* **153** 116150
[15] Tiedemann K, Tsao S and Komarova S V 2022 Platelets and osteoblasts: secretome connections *Am. J. Physiol. Cell Physiol.* **323** C347–53
[16] Liu J, Huang W, Pang Y, Zhu X, Zhou Y and Yan D 2010 The *in vitro* biocompatibility of self-assembled hyperbranched copolyphosphate nanocarriers *Biomaterials* **31** 5643–51
[17] Müller W E G, Wang X H, Diehl-Seifert B, Kropf K, Schloßmacher U, Lieberwirth I, Glasser G, Wiens M and Schröder H C 2011 Inorganic polymeric phosphate/polyphosphate as an inducer of alkaline phosphatase and a modulator of intracellular Ca^{2+} level in osteoblasts (SaOS-2 cells) *in vitro Acta Biomater.* **7** 2661–71
[18] Suess P M 2022 Effects of polyphosphate on leukocyte function *Prog. Mol. Subcell. Biol.* **61** 131–43
[19] Kuzmanov U, Gawri R, Zelinka A, Russell K A, Lee S H, Gramolini A and Kandel R 2021 Phosphoproteomic analysis of chondrocytes after short-term exposure to inorganic polyphosphate *bioRxiv* 2021 (https://doi.org/10.1101/2021.07.30.454470)
[20] Müller W E G, Wang S, Tolba E, Neufurth M, Ackermann M, Muñoz-Espí R, Lieberwirth I, Glasser G,

Schröder H C and Wang X H 2018 Transformation of amorphous polyphosphate nanoparticles into coacervate complexes: an approach for the encapsulation of mesenchymal stem cells *Small* **14** 1801170
[21] Schröder H C, Neufurth M, Zhou H, Wang S, Wang X H and Müller W E G 2022 Inorganic polyphosphate: coacervate formation and functional significance in nanomedical applications *Int. J. Nanomed.* **17** 5825–50
[22] Tseng Y H *et al* 2008 New role of bone morphogenetic protein 7 in brown adipogenesis and energy expenditure *Nature* **454** 1000–4
[23] Chen H and Zhang Y P J 2021 Enzymatic regeneration and conservation of ATP: challenges and opportunities *Crit. Rev. Biotechnol.* **41** 16–33
[24] Müller W E G, Schröder H C and Wang X H 2019 Inorganic polyphosphates as storage for and generator of metabolic energy in the extracellular matrix *Chem. Rev.* **119** 12337–74
[25] Verhoef J J *et al* 2017 Polyphosphate nanoparticles on the platelet surface trigger contact system activation *Blood* **129** 1707–17
[26] Choi S H, Smith S A and Morrissey J H 2011 Polyphosphate is a cofactor for the activation of factor XI by thrombin *Blood* **118** 6963–70
[27] Omelon S, Georgiou J, Variola F and Dean M N 2014 Colocation and role of polyphosphates and alkaline phosphatase in apatite biomineralization of elasmobranch tesserae *Acta Biomater.* **10** 3899–910
[28] Lipmann F 1941 Metabolic generation and utilization of phosphate bond energy *Advances in Enzymology and Related Subjects* vol 1 ed F F Nord and C H Werkman (Interscience Publishers) pp 99–162
[29] Müller W E G, Wang S, Neufurth M, Kokkinopoulou M, Feng Q, Schröder H C and Wang X H 2017 Polyphosphate as a donor of high-energy phosphate for the synthesis of ADP and ATP *J. Cell Sci.* **130** 2747–56
[30] Wilson C, Lee M D, Buckley C, Zhang X and McCarron J G 2022 Mitochondrial ATP production is required for endothelial cell control of vascular tone *Function* **4** zqac063
[31] Bernard K *et al* 2015 Metabolic reprogramming is required for myofibroblast contractility and differentiation *J. Biol. Chem.* **290** 25427–38
[32] Müller W E G, Ackermann M, Tolba E, Neufurth M, Ivetac I, Kokkinopoulou M, Schröder H C and Wang X H 2018 Role of ATP during the initiation of microvascularization. acceleration of an autocrine sensing mechanism facilitating chemotaxis by inorganic polyphosphate *Biochem. J.* **475** 3255–73
[33] Shin J Y, Yoon I-H, Kim J-S, Kim B and Park C-G 2009 Vascular endothelial growth factor-induced chemotaxis and IL-10 from T cells *Cell Immunol.* **256** 72–78
[34] Schepler H, Neufurth M, Wang S, She Z, Schröder H C, Wang X H and Müller W E G 2022 Acceleration of chronic wound healing by bio-inorganic polyphosphate: *in vitro* studies and first clinical applications *Theranostics* **12** 18–34
[35] U.S. Government 2023 Code of federal regulations—General provisions (available at: www.govinfo.gov/content/pkg/CFR-2023-title1-vol1/pdf/CFR-2023-title1-vol1.pdf) (Accessed 13 March 2023)
[36] Van Wazer J R 1958 *Phosphorus and Its Compounds* (Interscience Publishers)
[37] Ferrucci V *et al* 2021 Long-chain polyphosphates impair SARS-CoV-2 infection and replication *Sci. Signal* **14** eabe5040
[38] Müller W E G, Tolba E, Schröder H C, Wang S, Glaßer G, Muñoz-Espí R, Link T and Wang X H 2015 A new polyphosphate calcium material with morphogenetic activity *Mater. Lett.* **148** 166
[39] Müller W E G, Tolba E, Feng Q, Schröder H C, Markl J S, Kokkinopoulou M and Wang X H 2015 Amorphous Ca^{2+} polyphosphate nanoparticles regulate the ATP level in bone-like SaOS-2 cells *J. Cell Sci.* **128** 2202–7
[40] Neufurth M, Wang X H, Schröder H C, Feng Q, Diehl-Seifert B, Ziebart T, Steffen R, Wang S and Müller W E G 2014 Engineering a morphogenetically active hydrogel for bioprinting of bioartificial tissue derived from human osteoblast-like SaOS-2 cells *Biomaterials* **35** 8810–9
[41] Momeni A and Filiaggi M J 2013 Synthesis and characterization of different chain length sodium polyphosphates *J. Non-Cryst. Solids* **382** 11–17
[42] Oliver W C and Pharr G M 1992 An improved technique for determining hardness and elastic modulus using load and displacement sensing indentation experiments *J. Mater. Res.* **7** 1564–83
[43] Wisnom M R 2018 Size effects in composites *Comprehensive Composite Materials* vol 5 ed A Kelly and C Zweben (Pergamon) pp 23–47
[44] Christ J J, Willbold S and Blank L M 2020 Methods for the analysis of polyphosphate in the life sciences *Anal. Chem.* **92** 4167–76
[45] Li D, Frey M W and Joo Y L 2006 Characterization of nanofibrous membranes with capillary flow porometry *J. Membr. Sci.* **286** 104–15
[46] Ghasemi-Mobarakeh L, Prabhakaran M P, Morshed M, Nasr-Esfahani M-H and Ramakrishna S 2008 Electrospun poly(ε-caprolactone)/gelatin nanofibrous scaffolds for nerve tissue engineering *Biomaterials* **29** 4532–9
[47] Matko V 2004 Determination of porosity using a water pycnometer with capacitive level detection *Sens. Mater.* **16** 1–12
[48] Gloeckner H, Jonuleit T and Lemke H-D 2001 Monitoring of cell viability and cell growth in a hollow-fiber bioreactor by use of the dye Alamar blue *J. Immunol. Methods* **252** 131–8
[49] White K, Chalaby R, Lowe G, Berlin J, Glackin C and Olabisi R 2021 Calcein binding to assess mineralization in hydrogel microspheres *Polymers* **13** 2274
[50] Friedenstein A J, Petrakova K V, Kurolesova A I and Frolova G P 1968 Heterotopic of bone marrow. Analysis of precursor cells for osteogenic and hematopoietic tissues *Transplantation* **6** 230–47
[51] Pittenger M F, Mackay A M, Beck S C, Jaiswal R K, Douglas R, Mosca J D, Moorman M A, Simonetti D W, Craig S and Marshak D R 1999 Multilineage potential of adult human mesenchymal stem cells *Science* **284** 143–7
[52] Quarles L D, Yohay D A, Lever L W, Caton R and Wenstrup R J 1992 Distinct proliferative and differentiated stages of murine MC3T3-E1 cells in culture: an *in vitro* model of osteoblast development *J. Bone Min. Res.* **7** 683–92
[53] Wiens M, Wang X H, Schröder H C, Kolb U, Schloßmacher U, Ushijima H and Müller W E G 2010 The role of biosilica in the osteoprotegerin/RANKL ratio in human osteoblast-like cells *Biomaterials* **31** 7716–25
[54] Gregory C A, Grady Gunn W, Peister A and Prockop D J 2004 An Alizarin red-based assay of mineralization by adherent cells in culture: comparison with cetylpyridinium chloride extraction *Anal. Biochem.* **329** 77–84
[55] Wiens M, Wang X H, Schloßmacher U, Lieberwirth I, Glasser G, Ushijima H, Schröder H C and Müller W E G 2010 Osteogenic potential of bio-silica on human osteoblast-like (SaOS-2) cells *Calcif. Tissue Int.* **87** 513–24
[56] Schröder H C, Boreiko O, Krasko A, Reiber A, Schwertner H and Müller W E G 2005 Mineralization of SaOS-2 cells on enzymatically (Silicatein) modified bioactive osteoblast-stimulating surfaces *J. Biomed. Mater. Res. B* **75B** 387–92
[57] Khoo C P, Micklem K and Watt S M 2011 A comparison of methods for quantifying angiogenesis in the Matrigel assay *in vitro Tissue Eng. C* **17** 895–906
[58] Müller W E G, Ackermann M, Wang S, Neufurth M, Muñoz-Espí R, Feng Q, Schröder H C and Wang X H 2018 Inorganic polyphosphate induces accelerated tube formation of HUVEC endothelial cells *Cell Mol. Life Sci.* **75** 21–32
[59] Müller W E G, Neufurth M, Wang S, Schröder H C and Wang X H 2024 Polyphosphate nanoparticles: balancing

energy requirements in tissue regeneration processes *Small* **20** 2309528
[60] Docampo R and Moreno S N 2011 Acidocalcisomes *Cell Calcium* **50** 113–9
[61] Rey C *et al* 2011 Bioactive ceramics: physical chemistry *Comprehensive Biomaterials* vol 1 ed P Ducheyne, K Healy, D Hutmacher, D E Grainger and J Kirkpatrick (Elsevier) pp 187–221
[62] Chen E P, Toksoy Z, Davis B A and Geibel J P 2021 3D bioprinting of vascularized tissues for *in vitro* and *in vivo* applications *Front. Bioeng. Biotechnol.* **9** 664188
[63] Weiner S and Addadi L 1997 Design strategies in mineralized biological materials *J. Mater. Chem.* **7** 689–702
[64] Hu C, Xue Z, Wang X and Xu D 2019 Molecular dynamics exploration of the amorphous surface structures and properties of the biomimetic β-tricalcium phosphate *Appl. Surf. Sci.* **484** 72–82
[65] Zollo M *et al* 2021 SARS-CoV-2 subgenomic N (sgN) transcripts in Oro-nasopharyngeal swabs correlate with the highest viral load, as evaluated by five different molecular methods *Diagnostics* **11** 288
[66] Zhang Y, Sun N, Zhu M, Qiu Q, Zhao P, Zheng C, Bai Q, Zeng Q and Lu T 2022 The contribution of pore size and porosity of 3D printed porous titanium scaffolds to osteogenesis *Biomater. Adv.* **133** 112651
[67] Van Oosterwyck H, Duyck J, Vander Sloten J, Van der Perre G, De Coomans M, Lieven S, Puers R and Naert L 1998 The influence of bone mechanical properties and implant fixation upon bone loading around oral implants *Clin. Oral Implants Res.* **9** 407–18
[68] Strid K G 1985 Radiographic results *Tissue-integrated Prostheses* ed P-I Brånemark (Quintessence) pp 317–27
[69] Pawlikowski M, Skalski K, Bańczerowski J, Makuch A and Jankowski K 2017 Stress–strain characteristic of human trabecular bone based on depth sensing indentation measurements *Biocybern Biomed. Eng.* **37** 272–80
[70] Gerhardt L-C and Boccaccini A R 2010 Bioactive glass and glass-ceramic scaffolds for bone tissue engineering *Materials* **3** 3867–910
[71] Fu Q, Rahaman M N, Bal B S and Brown R F 2010 Preparation and in vitro evaluation of bioactive glass (13–93) scaffolds with oriented microstructures for repair and regeneration of load-bearing bones *J. Biomed. Mater. Res. A* **93** 1380–90
[72] Vimalraj S 2020 Alkaline phosphatase: structure, expression and its function in bone mineralization *Gene* **754** 144855
[73] Tudureanu R, Handrea-Dragan I M, Boca S and Botiz I 2022 Insight and recent advances into the role of topography on the cell differentiation and proliferation on biopolymeric surfaces *Int. J. Mol. Sci.* **23** 7731
[74] Hanna H, Mir L M and Andre F M 2018 In vitro osteoblastic differentiation of mesenchymal stem cells generates cell layers with distinct properties *Stem Cell Res. Ther.* **9** 203
[75] Langenbach F and Handschel J 2013 Effects of dexamethasone, ascorbic acid and β-glycerophosphate on the osteogenic differentiation of stem cells in vitro *Stem Cell Res. Ther.* **4** 117
[76] Murad S, Grove D, Lindberg K A, Reynolds G, Sivarajah A and Pinnell S R 1981 Regulation of collagen synthesis by ascorbic acid *Proc. Natl Acad. Sci. USA* **78** 2879–82
[77] Wang H, Pang B, Li Y, Zhu D, Pang T and Liu Y 2012 Dexamethasone has variable effects on mesenchymal stromal cells *Cytotherapy* **14** 423–30
[78] Wang X H, Schröder H C, Wiens M, Ushijima H and Müller W E G 2012 Bio-silica and bio-polyphosphate: applications in biomedicine (bone formation) *Curr. Opin. Biotechnol.* **23** 570–8
[79] Viguet-Carrin S, Garnero P and Delmas P D 2006 The role of collagen in bone strength *Osteoporos Int.* **17** 319–36
[80] Christenson R H 1997 Biochemical markers of bone metabolism: an overview *Clin. Biochem.* **30** 573–93
[81] Liebig B E, Kisiday J D, Bahney C S, Ehrhart N P and Goodrich L R 2020 The platelet-rich plasma and mesenchymal stem cell milieu: a review of therapeutic effects on bone healing *J. Orthop. Res.* **38** 2539–50
[82] Pettersson L F, Kingham P J, Wiberg M and Kelk P 2017 *In vitro* osteogenic differentiation of human mesenchymal stem cells from jawbone compared with dental tissue *Tissue Eng. Regen. Med.* **14** 763–74
[83] Rashid U, Becker S K, Sponder G, Trappe S, Sandhu M A and Aschenbach J R 2023 Low magnesium concentration enforces bone calcium deposition irrespective of 1,25-dihydroxyvitamin D3 concentration *Int. J. Mol. Sci.* **24** 8679
[84] Oliveros Anerillas L, Kingham P J, Lammi M J, Wiberg M and Kelk P 2021 Three-dimensional osteogenic differentiation of bone marrow mesenchymal stem cells promotes matrix metallopeptidase 13 (MMP13) expression in type I collagen hydrogels *Int. J. Mol. Sci.* **22** 13594
[85] Bohner M, Santoni B L G and Döbelin N 2020 β-tricalcium phosphate for bone substitution: synthesis and properties *Acta Biomater.* **113** 23–41
[86] Yuan H, Fernandes H, Habibovic P, de Boer J, Barradas A M C, de Ruiter A, Walsh W R, van Blitterswijk C A and de Bruijn J D 2010 Osteoinductive ceramics as a synthetic alternative to autologous bone grafting *Proc. Natl Acad. Sci. USA* **107** 13614–9
[87] Bohner M and Miron R J 2019 A proposed mechanism for material-induced heterotopic ossification *Mater. Today* **22** 132–41
[88] Huang Z, Li J, He B, Lu B, Li Y, Zhang R, Lu J, Wang Z and Li X 2024 Enhancing mechanical performance of hydroxyapatite-based bone implants via citric acid post-processing in binder jetting additive manufacturing *Biomed. Mater.* **19** 065020
[89] Frank Gladson T S, Ramesh R and Kavitha C 2019 Experimental investigation of mechanical, tribological and dielectric properties of alumina nano wire-reinforced PEEK/PTFE composites *Mater. Res. Express* **6** 115327
[90] Uysal I, Tezcaner A and Evis Z 2024 Tezcaner A and Evis Z 2024 Methods to improve antibacterial properties of PEEK: a review *Biomed. Mater.* **19** 022004
[91] Barradas A M, Yuan H, van Blitterswijk C A and Habibovic P 2011 Osteoinductive biomaterials: current knowledge of properties, experimental models and biological mechanisms *Eur. Cell. Mater.* **21** 407–29
[92] Friedenstein A Y 1968 Induction of bone tissue by transitional epithelium *Clin. Orthop. Relat. Res.* **59** 21–37
[93] Fujihara C, Nantakeeratipat T and Murakami S 2022 Energy metabolism in osteogenic differentiation and reprogramming: a possible future strategy for periodontal regeneration *Front. Dent. Med.* **3** 815140
[94] Lin X, Patil S, Gao Y-G and Qian A 2020 The bone extracellular matrix in bone formation and regeneration *Front. Pharmacol.* **11** 757
[95] Feng L-L, Cai Y-Q, Zhu M-C, Xing L-J and Wang X 2020 The yin and yang functions of extracellular ATP and adenosine in tumor immunity *Cancer Cell Int.* **20** 110
[96] Partridge E, Hicks V and Smith G 1941 W A thermal, microscopic and x-ray study of the system $NaPO_3$–$Na_4P_4O_3$ *J. Am. Chem. Soc.* **63** 454–66
[97] Bobyn J D, Pilliar R M, Cameron H U and Weatherly G C 1980 The optimum pore size for the fixation of porous-surfaced metal implants by the ingrowth of bone *Clin. Orthop. Relat. Res.* **150** 263–70
[98] Wang Z, Wang C, Li C, Qin Y, Zhong L, Chen B, Li Z, Liu H, Chang F and Wang J 2017 Analysis of factors influencing bone ingrowth into three-dimensional printed porous metal scaffolds: a review *J. Alloys Compd.* **717** 271–85
[99] Dabrowski B, Swieszkowski W, Godlinski D and Kurzydlowski K J 2010 Highly porous titanium scaffolds for orthopaedic applications *J. Biomed. Mater. Res. B* **95** 53–61

[100] Dickens B, Schroeder L and Brown W 1974 Crystallographic studies of the role of Mg as a stabilizing impurity in β-$Ca_3(PO_4)_2$. The crystal structure of pure β-$Ca_3(PO_4)_2$ *J. Solid State Chem.* **10** 232–48
[101] Siemon N J and Moodie E W 1974 Reproducibility of specific gravity estimations on bone samples from different sites of cattle and sheep *Calcif Tissue Res.* **15** 181–8
[102] Morgan E F, Unnikrisnan G U and Hussein A I 2018 Bone mechanical properties in healthy and diseased states *Annu. Rev. Biomed. Eng.* **20** 119–43
[103] Müller W E G, Ackermann M, Al-Nawas B, Righesso L A R, Muñoz-Espí R, Tolba E, Neufurth M, Schröder H C and Wang X H 2020 Amplified morphogenetic and bone forming activity of amorphous versus crystalline calcium phosphate/polyphosphate *Acta Biomater.* **118** 233–47
[104] Chen J B, Diane A, Lyman S, Chiu Y-F, Blevins J L and Westrich G H 2022 Predicting implant size in total hip arthroplasty *Arthroplast. Today* **15** 210–4
[105] Shiba T, Tsutsumi K, Yano H, Ihara Y, Kameda A, Tanaka K, Takahashi H, Munekata M, Rao N N and Kornberg A 1997 Inorganic polyphosphate and the induction of rpoS expression *Proc. Natl Acad. Sci. USA* **94** 11210–5
[106] Rao N N, Gómez-García M R and Kornberg A 2009 Inorganic polyphosphate: essential for growth and survival *Annu. Rev. Biochem.* **78** 605–47
[107] Foster K G and Fingar D C 2010 Mammalian target of rapamycin (mTOR): conducting the cellular signaling symphony *J. Biol. Chem.* **285** 14071–7
[108] Müller W E G, Schepler H, Neufurth M, Dobmeyer R, Batel R, Schröder H C and Wang X H 2024 Energy level as a theranostic factor for successful therapy of tissue injuries with polyphosphate: the triad metabolic energy—mechanical energy—heat *Theranostics* **14** 5262–80
[109] Reddy R and Reddy N 2018 Biomimetic approaches for tissue engineering *J. Biomater. Sci. Polym. Ed.* **29** 1667–85
[110] Filippi M, Born G, Chaaban M and Scherberich A 2020 Natural polymeric scaffolds in bone regeneration *Front. Bioeng. Biotechnol.* **8** 474
[111] Discher D E, Mooney D J and Zandstra P W 2009 Growth factors, matrices, and forces combine and control stem cells *Science* **324** 1673–7
[112] Müller W E G, Schepler H, Neufurth M, Wang S, Ferrucci V, Zollo M, Tan R, Schröder H C and Wang X H 2023 The physiological polyphosphate as a healing biomaterial for chronic wounds: crucial roles of its antibacterial and unique metabolic energy supplying properties *J. Mater. Sci. Technol.* **135** 170–85
[113] Alkaabi S A *et al* 2021 Safety and feasibility study of using polyphosphate (PolyP) in alveolar cleft repair: a pilot study *Pilot Feasibility Stud.* **7** 199
[114] European Parliament and of the Council 2008 Regulation (EC) No 1333/2008 of the European parliament and of the council of 16 December 2008 on food additives Off *J. Eur. Union* **L354** 16–33
[115] Groeneveld M C, Van den Bos T, Everts V and Beertsen W 1996 Cell-bound and extracellular matrix-associated alkaline phosphatase activity in rat periodontal ligament *J. Periodontal. Res.* **31** 73–79
[116] Zeiner J *et al* 2019 Soluble and membrane-bound adenylate kinase and nucleotidases augment ATP-mediated inflammation in diabetic retinopathy eyes with vitreous hemorrhage *J. Mol. Med.* **97** 341–54